Bridging the gap between simulated and experimental ionic conductivities in lithium superionic conductors

J. Qi [a], S. Banerjee [b], Y. Zuo [b], C. Chen [b], Z. Zhu [b], M.L. Holekevi Chandrappa [b], X. Li [b], S.P. Ong [b, *]

[a] Materials Science and Engineering Program, University of California San Diego, 9500 Gilman Dr, Mail Code 0448, La Jolla, CA, 92093-0448, United States
[b] Department of NanoEngineering, University of California San Diego, 9500 Gilman Dr, Mail Code 0448, La Jolla, CA, 92093-0448, United States

ARTICLE INFO

ABSTRACT

Lithium superionic conductors (LSCs) are of major importance as solid electrolytes for next-generation all-solid-state lithium-ion batteries. While *ab initio* molecular dynamics have been extensively applied to study these materials, there are often large discrepancies between predicted and experimentally measured ionic conductivities and activation energies due to the high temperatures and short time scales of such simulations. Here, we present a strategy to bridge this gap using moment tensor potentials (MTPs). We show that MTPs trained on energies and forces computed using the van der Waals optB88 functional yield much more accurate lattice parameters, which in turn leads to accurate prediction of ionic conductivities and activation energies for the $Li_{0.33}La_{0.56}TiO_3$, Li_3YCl_6 and $Li_7P_3S_{11}$ LSCs. NPT MD simulations using the optB88 MTPs also reveal that all three LSCs undergo a transition between two quasi-linear Arrhenius regimes at relatively low temperatures. This transition can be traced to an increase in the number and diversity of diffusion pathways, in some cases with a change in the dimensionality of diffusion. This work presents not only an approach to develop high accuracy MTPs, but also outlines the diffusion characteristics for LSCs which is otherwise inaccessible through *ab initio* computation.

© 2021 Elsevier Ltd. All rights reserved.

1. Introduction

Lithium superionic conductors (LSCs) are the critical enabling solid electrolyte component in next-generation all-solid-state rechargeable lithium-ion batteries [1–4]. Replacing the traditional flammable organic solvent electrolyte, ceramic LSCs exhibit superior safety and are also a potential pathway to higher energy density cell architectures and utilization of lithium metal anodes. As the name implies, a key property of LSCs is a high ionic conductivity, typically ranging from O (10^{-1}) mS cm^{-1} to O (10) mS cm^{-1} (rivaling that of liquid electrolytes) at room temperature. The anion chemistry of an LSC has a major influence on their properties. Sulfide LSCs, such as the $Li_{10}GeP_2S_{12}$ (LGPS) family [5–8], $Li_7P_3S_{11}$ [9–13] and Li_3PS_4 [14–16], tend to have very high ionic conductivities due to the large, polarizable S^{2-}, but suffer from narrow electrochemical stability windows, air- and moisture-sensitivity.

Oxide LSCs, such as the $Li_7La_3Zr_2O_{12}$ garnet family [17] and LISICONs [18–20], typically have lower ionic conductivities compared to the sulfides, but are much more electrochemically and chemically stable. Recently, a promising new class of halide LSCs, Li_3YCl_6 and Li_3YBr_6, has been discovered that exhibits a good compromise of ionic conductivities (0.51 mS cm^{-1} for Li_3YCl_6 and 1.7 mS cm^{-1} for Li_3YBr_6) and electrochemical stabilities between those of the sulfides and oxides [21].

Molecular dynamics (MD) simulations have been extensively used in the study of ion conduction in LSCs and other materials. In particular, *ab initio* MD (AIMD), i.e., simulations where the energies and forces are directly obtained by solving the Schrödinger equation via density functional theory (DFT), have emerged as a powerful tool in recent years as they can be transferably applied to the entire range of LSC chemistries [13,22–29]. However, the high cost of AIMD simulations means that they are usually performed at elevated temperatures to obtain sufficient diffusion statistics, sometimes far in excess of the melting points of some LSCs, and for relatively short simulation time frames (~ 100 ps). As a consequence, extrapolated room-temperature ionic conductivity and

diffusivity have large error bars [30]. Further, there may be phase transitions or transitions in diffusion mechanisms occurring between room temperature and high simulation temperatures, invalidating the Arrhenius assumption used in extrapolation. Such non-Arrhenius behavior and phase transitions have been reported in many LSCs, including $Li_{3x}La_{2/3-x}TiO_3$ [31,32], Li_3PS_4 [14], and LGPS [33]. Another source of error arises from the fact that most AIMD simulations of LSCs are performed in the NVT ensemble using the equilibrium volume from a 0 K density functional theory (DFT) relaxation calculation. The most common DFT functional used is the Perdew-Burke-Ernzerhof (PBE) generalized gradient approximation (GGA) [34], which tends to overestimate the lattice parameters of solids and differ from experimental values by up to 2−3% [35,36]. These differences in lattice parameters can have a major effect on ion diffusion and activation barriers [23,37].

The net result of the mismatch in working temperatures and lattice parameters between simulations and experiments is that room-temperature ionic diffusivity and conductivity of LSCs computed from AIMD simulations often disagree substantially with those measured experimentally, e.g., via electrochemical impedance spectroscopy (EIS). For example, Chu et al. [13] previously predicted a room-temperature ionic conductivity of 57 mS cm^{-1} for the $Li_7P_3S_{11}$ LSC using AIMD simulations, far in excess of the highest experimentally measured room-temperature ionic conductivity of 17 mS cm^{-1} [10]. Similarly, Wang et al. [29] predicted an ionic conductivity of 14 mS cm^{-1} for the Li_3YCl_6 LSC, again far in excess of the experimentally reported 0.51 mS cm^{-1} [21].

Classical MD simulations using an interatomic potential (IAP) to parameterize the potential energy surface (PES) are a potential solution to enable low-temperature and long-timescale studies. In recent years, machine learning (ML) the PES as a function of local environment descriptors has emerged as an especially promising, and reproducible approach to develop IAPs with near-DFT accuracy in energies and forces [38−50]. However, most ML-IAPs that have been developed in the literature still rely on DFT calculations performed using the PBE functional; as such, their performance are still limited by the accuracy of the DFT training data.

In this work, we show that the gap between experimental and simulated ionic conductivities in LSCs can be bridged by developing ML-IAPs under the moment tensor potential (MTP) formalism [41,51] using training data from the optB88 van der Waals (vdW) DFT functional [36,52]. Three LSCs, $Li_{0.33}La_{0.56}TiO_3$ (LLTO), Li_3YCl_6 and $Li_7P_3S_{11}$ spanning a diversity of anion chemistries have been selected as the model systems for investigation, as shown in Fig. 1. These LSCs have been selected because of their major interest to the battery research community, as well as the fact that previous AIMD calculations have either yielded large disagreements with experimentally reported room temperature conductivity or else have not been performed as in the case of LLTO. We demonstrate that in all three cases, the discrepancy between computed and measured conductivities can be explained by a transition between quasilinear Arrhenius regimes arising from the activation of additional diffusion pathways.

2. Material and methods

Fig. 2 summarizes the overall workflow for the construction of MTPs for the LSCs investigated in this work as well as the DFT functional choices investigated.

2.1. Structure construction

Supercells of LLTO, Li_3YCl_6 and $Li_7P_3S_{11}$ with lattice parameters greater than 10 Å were constructed to minimize interactions between periodic images. For LLTO, a $3 \times 3 \times 1$ supercell of LLTO,
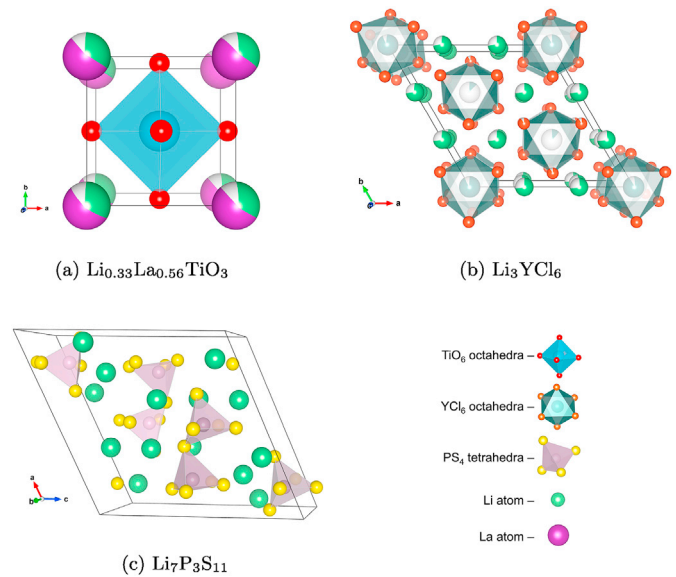

(a) $Li_{0.33}La_{0.56}TiO_3$

(b) Li_3YCl_6

(c) $Li_7P_3S_{11}$

TiO$_6$ octahedra –

YCl$_6$ octahedra –

PS$_4$ tetrahedra –

Li atom –

La atom –

Fig. 1. Crystal structures of (a) $Li_{0.33}La_{0.56}TiO_3$ (Space group $Pm\bar{3}m$, No. 221), (b) Li_3YCl_6 (Space group $P\bar{3}m1$, No. 164), and (c) $Li_7P_3S_{11}$(Space group $P1$, No. 2).

equivalent to $x = 0.11$ in the general formula of $Li_{3x}La_{2/3-x}TiO_3$ [31,53,54], was initially generated to enumerate symmetrically distinct orderings of Li/La/Vacancy on the perovskite A site. These orderings were fully relaxed by DFT. The lowest energy ordering was then stacked along the c direction to obtain a $3 \times 3 \times 3$ supercell with 132 atoms. During relaxation, shifts of the lithium ion position from the A-sites of perovskite were observed (see Figure S1), which is consistent with previous theoretical studies on LLTO [55−57]. Li_3YCl_6 has previously been identified to be an isomorph of Li_3ErCl_6 (ICSD No. 50151, space group $P\bar{3}m1$, No. 164) [21]. Starting from the experimentally reported disordered Li_3YCl_6 structure, the site occupancies were rounded to the nearest rational numbers based on a total of 3 formula units per unit cell (see Table S1) and enumeration of distinct orderings was performed. The lowest energy relaxed structure was then selected to construct a $1 \times 1 \times 2$ supercell with 60 atoms. A $1 \times 2 \times 1$ supercell of $Li_7P_3S_{11}$ with 84 atoms was constructed from the experimentally refined crystal structure [9]. The formation energies (E_f) and energy above the convex hull (E_{hull}) for all three LSCs calculated with the PBE and optB88 functionals are given in Table S2. All three LSCs are predicted to have $E_{hull} < 0.05$ eV/atom. The optB88 E_f are 5−10% lower than the PBE values, which is consistent with the ~5% higher atomization energies predicted by optB88 for ionic solids [36].

2.2. DFT calculations and AIMD simulations

All DFT calculations were performed using the Vienna *ab initio* simulation package (VASP) with the projector augmented-wave (PAW) approach [58,59]. For initial structural relaxations (Step 1 in Fig. 2), spin-polarized calculations were performed with an energy cutoff of 520 eV and a k-point density of at least 64/A^{-3}, similar to those used in the Materials Project (MP) [60].

In Step 2, non-spin polarized *ab initio* molecular dynamics (AIMD) simulations using NVT ensemble were carried out on the relaxed supercells with a plane-wave energy cutoff of 280 eV and a minimal Γ-centered $1 \times 1 \times 1$ k-mesh. A time step of 2 fs and the Nose−Hoover thermostat [61,62] were used. A similar protocol was followed as previous works [45,46,48], wherein simulations were performed at three strains (0, ±0.05) and four temperatures
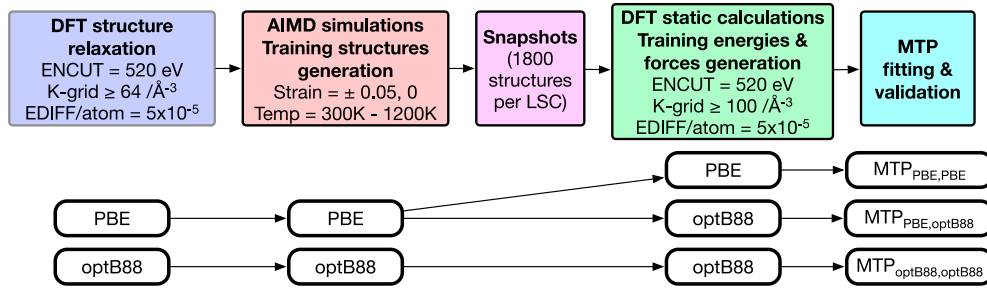
Fig. 2. Flowchart of the stepwise construction of MTPs for LSCs. DFT functionals utilized in each step and the names of the as-trained MTPs were listed.

(300 K–1200 K with 300 K intervals) to diversify the training structures. The initial structures were heated from 0 K to the target temperatures with a temperature gradient of 0.25 K/fs and equilibrated for at least 30 ps. Snapshots were then extracted from a production run of 15 ps at 0.1 ps intervals, i.e., 150 structures for each temperature and strain. Hence, for each LSC, a total of 1800 training structures (150 × 4 temperatures × 3 strains) were generated.

In Step 3, static self-consistent calculations were performed on the training structures to obtain accurate energies and forces for MTP training. These calculations were performed with a higher k-point density of at least $100/A^{-3}$, an energy cutoff of 520 eV and an electronic relaxation convergence condition of 5×10^{-5} eV/atom, which were consistent with those used in MP [60].

A main goal of this work is to evaluate the choice of the DFT functional on the training data and hence, the performance of the MTP generated. The initial structural relaxations and energy evaluations of symmetrically distinct LLTO and Li_3YCl_6 orderings were performed using the PBE [34] functional. Subsequent structural relaxations, AIMD simulations and static energy valuations were performed using either the PBE functional or optB88 vdW functional [36,52], as shown in Fig. 2.

All DFT and AIMD simulations were carried out using fully-automated workflows [28] built on the Python Materials Genomics (pymatgen) [63] library and FireWorks scientific workflow package [64].

2.3 MTP. model training and verification

The moment tensor potential (MTP) formalism has been extensively discussed in earlier works [41,48,51] and successfully applied to many chemical systems, including metals [41,48,65], boron [66], alloys [51], gas-phase reactions [67] and cathode coating materials [49]. Briefly, the MTP describes the local environment around each atom in terms of moment tensors $M_{\mu,\nu}$, defined as follows:

$$M_{\mu,\nu}(\mathbf{n_i}) = \sum_j f_\mu(|\mathbf{r_{ij}}|, z_i, z_j) \underbrace{\mathbf{r_{ij}} \otimes \ldots \otimes \mathbf{r_{ij}}}_{\nu times} \qquad (1)$$

Here, $\mathbf{n_i}$ denotes the atomic types as well as the relative positions of the ith atom and all of its neighboring atoms. z_i and z_j represent the atomic types (integers from 0 to n-1 for a system with n different types of atoms) of the ith atom and its jth neighbor, respectively, and $\mathbf{r_{ij}}$ is the position vector of the jth neighbor to the ith atom. The radial part of the atomic environment is given by the f_μ term, and the angular part is encoded by the outer product ($\otimes$) of the $\mathbf{r_{ij}}$ vectors, which is a tensor with rank ν. The moment tensors $M_{\mu,\nu}$ are then contracted to basis functions B_α, which are intrinsically invariant to atomic permutations, rotations and reflections. The energy of the system E_{MTP} is then expressed as a linear function of B_α as follows:

$$E_{MTP} = \sum_{i=1}^n \sum_\alpha \xi_\alpha B_\alpha(\mathbf{n_i}) \qquad (2)$$

where n and α are the total number of atoms inside the system and the total number of basis functions for each atom, respectively, and ξ_α are the coefficients fitted in the training process implemented in the MLIP package. Similarly, the forces and stresses can be expressed as the first and second derivatives of the E_{MTP} with respect to $\mathbf{r_{ij}}$ [41,51]. An optimized MTP is then obtained by minimizing the errors in the predicted energies and forces with respect to the DFT training data. In this work, the energy and force data points are assigned weights of 100:1, similar to previous works [45–48].

Two key parameters control the performance trade-off of the MTP. The radius cutoff R_{cut} determines the maximum interaction range between atoms. The larger the R_{cut}, the more the atomic interactions encoded in Equation (1). The completeness of the basis functions B_α is controlled by its maximum level (lev_{max}). The larger the lev_{max}, the larger the number of terms in the linear expansion in Equation (2), which in turn results in higher computational cost and a greater likelihood of over-fitting. In this work, the R_{cut} was chosen to be 5.0 Å, a typical value used in previously reported MTPs [49,51,68], while the lev_{max} were set as 18 for Li_3YCl_6 and $Li_7P_3S_{11}$ and 16 for LLTO based on our convergence tests (see Figure S2-S5). For the fitting, a training:test split of 90:10 was used. In total, seven MTPs were fitted for LLTO, Li_3YCl_6 and $Li_7P_3S_{11}$ according to the above discussed procedure. These MTPs are labeled with subscripts indicating the functionals used during the AIMD simulation (Step 2) and static energies and forces evaluations (Step 3). For instance, $MTP_{PBE, optB88}$ refers to an MTP fitted using the snapshots extracted from AIMD simulations performed using the PBE functional, with energies and forces evaluated using the optB88 functional. It should be noted that $MTP_{optB88, optB88}$ was fitted only for $Li_7P_3S_{11}$ as a test case and because the results were highly similar to $MTP_{PBE, optB88}$ (see later Results section), only the latter was fitted for the other two LSCs. Previously, the current authors have also used an alternative approach in which the long-ranged electrostatic interactions were accounted for separately via an Ewald summation of the formal oxidation states prior to fitting the residual interactions via the ML-IAP [46]. A similar "electrostatic" MTP (eMTP) for the LLTO LSC was also developed but the performance was similar to the MTP without separate accounting of electrostatics. It can be concluded that there is significant screening in these materials, and the radius cutoff used above is already sufficient to account for most of the electrostatic interactions (see Figure S6).

All training, evaluations and simulations with MTP were performed using MLIP [41,51], LAMMPS [69] and the open-source Materials Machine Learning (maml) Python package [70].

2.4. QHA thermal expansion

Phonon calculations were performed using the supercells (outlined in Section 2.1) at nine fixed volumes (80%−120% with 5% intervals of the equilibrium volume at 0 K from structural relaxations with PBE and optB88 functionals). Real-space force constants were calculated utilizing the density functional perturbation theory (DFPT) [71] method as implemented in VASP, while the real-space force constants from MTPs were generated with the finite displacement approach implemented in the Phonopy [72] package. Phonon frequencies were then calculated from the force constants, and the thermal expansion from 0 K to 800 K was calculated under the quasi-harmonic approximation (QHA).

2.5. Diffusivity and conductivity calculations

Classical MD simulations for each LSC were performed using the trained MTPs. Taking advantage of the lower computational cost and linear scaling of MTP calculations with respect to system size, larger supercells with all lattice parameters over 20 Å were used for these simulations. Based on benchmarks of the convergence of the ionic conductivity with cell sizes (Figure S7), simulation cells of $3 \times 3 \times 2$ (2,376 atoms), $2 \times 2 \times 3$ (720 atoms) and $3 \times 2 \times 2$ (1,008 atoms) AIMD supercells are utilized for LLTO, Li_3YCl_6 and $Li_7P_3S_{11}$, respectively. The time step was set to 1 fs, and the total simulation time was at least 1 ns for all MD simulations.

The tracer diffusivity (D^*) of Li ions was obtained by performing a linear fitting of the mean square displacement (MSD) of all diffusing Li ions with time, according to the Einstein relation [73]:

$$D^* = \frac{1}{2dNt} \sum_{i=1}^{N} [\Delta r_i(t)]^2 \tag{3}$$

where d is the number of dimensions in which diffusion occurs ($d = 3$ for all three electrolytes), N is the total number of diffusing Li ions, and $\Delta r_i(t)$ is the displacement of the ith Li ion at time t.

The charge diffusivity (D_σ) of Li ions was calculated from the square net displacement of all diffusing Li ions, as described below [73]:

$$D_\sigma = \frac{1}{2dNt} \left[\sum_{i=1}^{N} \Delta r_i(t) \right]^2 \tag{4}$$

The Haven ratio is then given by the following equation:

$$H_R = D^*/D_\sigma \tag{5}$$

Finally, the ionic conductivity $\sigma(T)$ at temperature T is given by the Nernst-Einstein equation [73]:

$$\sigma(T) = \frac{\rho z^2 F^2}{RT} D_\sigma(T) \tag{6}$$

where ρ is the molar density of diffusing ions in the unit cell, z, F and R are the charge of Li ions ($z = 1$), the Faraday constant and the gas constant, respectively. Arrhenius plots were then generated to determine the temperature-dependent activation energies (E_a).

3. Results

3.1. MTP validation

Table 1 compares the mean absolute errors (MAEs) in energies and forces of the fitted MTPs. In all cases, the MAEs in energies are between 0.96 meV/atom and 2.07 meV/atom, while the MAEs in

Table 1
Mean absolute errors (MAEs) on energies and forces predictions for fitted MTPs. The MAEs were calculated with respect to static energies and forces from the respective DFT functionals.

LSC	MTP	MAE$_{energies}$ (meV/atom)		MAE$_{forces}$ (eV/Å)	
		Training	Test	Training	Test
LLTO	MTP$_{PBE, PBE}$	1.40	1.44	0.12	0.12
	MTP$_{PBE, optB88}$	1.39	1.24	0.10	0.10
Li_3YCl_6	MTP$_{PBE, PBE}$	0.96	1.11	0.04	0.04
	MTP$_{PBE, optB88}$	1.00	1.06	0.04	0.04
$Li_7P_3S_{11}$	MTP$_{PBE, PBE}$	1.77	1.92	0.09	0.08
	MTP$_{PBE, optB88}$	1.70	1.78	0.08	0.08
	MTP$_{optB88, optB88}$	1.79	2.07	0.09	0.09

forces are below 0.20 eV/Å. These MAEs are similar to or lower than those of other MTPs fitted in the literature [48,49], and a substantial improvement over traditional IAPs. The training and test MAEs are generally very similar, indicating that there is little likelihood of overfitting. The MAEs in energies and forces are also uniformly distributed with respect to the different temperatures that training structures were extracted from (see Figure S3-S5), indicating consistently high accuracy of our MTPs to reproduce DFT energies and forces at different temperatures. These results are consistent regardless of the DFT functionals (PBE or optB88) used to generate the training data. Further analysis also found that the local environments sampled by nanosecond NPT MD simulations using the fitted MTP are similar with those sampled by the AIMD training data (Figure S8) and the MAEs in forces are consistently low regardless of local environment (Figure S9). It should be noted that while it is possible that MD simulations under more extreme conditions, e.g., above 1200 K, may sample local environments that are substantially different from the AIMD training data and possibly result in higher errors, such conditions are unlikely to be of interest for most applications of the fitted MTPs.

3.2. Lattice parameters

Table 2 compares the lattice parameters and volumes for the three LSCs from DFT and MTP relaxations with experimental values. It can be seen that the use of the optB88 functional significantly improves the predicted lattice parameters and densities over the PBE functional for Li_3YCl_6 and $Li_7P_3S_{11}$ LSCs, while yielding smaller improvements for LLTO LSC. The PBE computed densities underestimate the experimental densities by 3−6%, consistent with the well-known propensity of PBE to underbind. The optB88 computed densities are within 1−3% of the experimental densities due to the fact that optB88 functional is less repulsive at short interatomic separations [36]. As shown in Fig. 3, the MTPs are generally able to reproduce the DFT lattice parameters to within 1−2.5%. It should be noted that the errors with respect to DFT follows the order LLTO < Li_3YCl_6~$Li_7P_3S_{11}$. We hypothesize that this can be attributed to the difference in the potential energy landscapes, *i.e.*, Li_3YCl_6 and $Li_7P_3S_{11}$ have shallower potential energy landscapes, which leads to smaller energy changes with lattice parameter variations. This can be seen to some degree in the equation of state plots (see later Fig. 4), as the same percentage of change in volume leads to smaller changes in the total energies of Li_3YCl_6 and $Li_7P_3S_{11}$.

3.3. Equations of state and thermal expansion

Fig. 4a−c shows the equation of state (EOS) curves of the three LSCs calculated from DFT and MTPs. In general, the MTP computed EOSs agree well with the corresponding DFT EOSs, further attesting

Table 2

Lattice parameters and densities of LSCs relaxed with the PBE and optB88 DFT functionals and the trained MTPs at 0 K, in comparison with experimental lattice parameters and densities at room temperature for LLTO [53], Li_3YCl_6 [21] and $Li_7P_3S_{11}$ [9]. Values in brackets are the percentage differences between the computed values and the experimental measurements.

	a (Å)	b (Å)	c (Å)	Density (g cm^{-3})
LLTO				
DFT PBE	3.96 (2.3%)	3.89 (0.5%)	3.91 (1.0%)	4.84 (−3.0%)
DFT optB88	3.95 (2.1%)	3.88 (0.3%)	3.90 (0.8%)	4.88 (−2.2%)
MTP$_{PBE, PBE}$	3.96 (2.3%)	3.89 (0.5%)	3.90 (0.8%)	4.85 (−2.8%)
MTP$_{PBE, optB88}$	3.95 (2.1%)	3.87 (0.0%)	3.89 (0.5%)	4.90 (−1.8%)
Experiment	3.87	3.87	3.87	4.99
Li_3YCl_6				
DFT PBE	11.17 (−0.3%)	11.17 (−0.3%)	6.22 (3.2%)	2.37 (−3.3%)
DFT optB88	11.01 (−1.7%)	11.01 (−1.7%)	6.02 (−0.2%)	2.52 (2.9%)
MTP$_{PBE, PBE}$	11.18 (−0.2%)	11.18 (−0.2%)	6.27 (4.0%)	2.35 (−4.1%)
MTP$_{PBE, optB88}$	11.04 (−1.4%)	11.04 (−1.4%)	6.08 (0.8%)	2.48 (1.2%)
Experiment	11.20	11.20	6.03	2.45
$Li_7P_3S_{11}$				
DFT PBE	12.86 (2.9%)	6.19 (2.7%)	12.69 (1.3%)	1.87 (−5.6%)
DFT optB88	12.61 (0.9%)	6.08 (0.8%)	12.62 (0.7%)	1.95 (−1.5%)
MTP$_{PBE, PBE}$	12.66 (1.3%)	6.33 (5.0%)	12.56 (0.2%)	1.88 (−5.1%)
MTP$_{PBE, optB88}$	12.52 (0.2%)	6.14 (1.8%)	12.57 (0.3%)	1.95 (−1.5%)
MTP$_{optB88, optB88}$	12.52 (0.2%)	6.12 (1.5%)	12.66 (1.0%)	1.96 (−1.0%)
Experiment	12.50	6.03	12.53	1.98

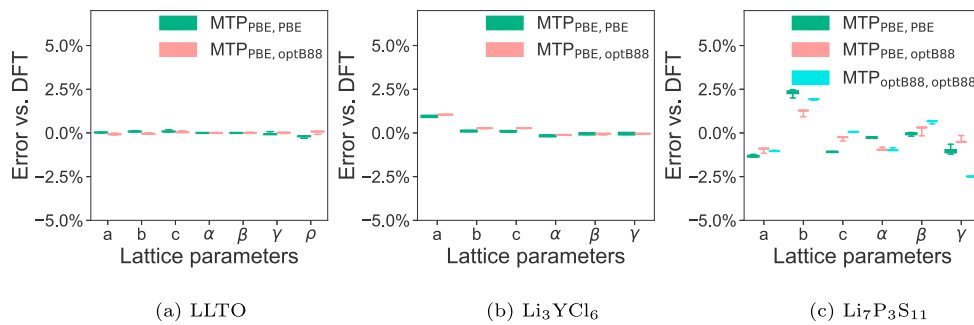(a) LLTO   (b) Li_3YCl_6 (c) $Li_7P_3S_{11}$

Fig. 3. Comparison of the lattice parameters predicted via relaxation with the trained MTPs and the DFT-relaxed values. For each MTP, the relaxation was performed using 36 strained structures constructed by applying strains of −0.15 to 0.15 with 0.05 intervals in six different modes to the DFT relaxed ground-state structure to assess the numerical stability of MTP relaxation.

to the robustness of the MTP fitting procedure. In addition to the differences in equilibrium volumes discussed in the preceding section, we note that the optB88 DFT and MTP calculations predict a larger curvature for Li_3YCl_6 and $Li_7P_3S_{11}$ LSCs, i.e., the optB88 functional predicts a higher bulk modulus than PBE. These results are consistent with the calculated QHA thermal volume expansion, plotted in Fig. 4d–f. The MTP QHA thermal expansion curves match closely with the corresponding DFT QHA thermal expansion curves. In general, the optB88 DFT and MTP volumes are much closer to the experimental volumes for respective temperatures between 0 and 800 K. LLTO has the smallest MTP$_{PBE, optB88}$ vol expansion coefficient ($\beta_{PBE,optB88}$) of 1.08×10^{-5} K^{-1} from 300 K to 800 K, in excellent agreement with the reported low thermal expansion coefficient of 9.35×10^{-6} K^{-1} from X-ray diffraction analysis from 298 K to 800 K [74]. Li_3YCl_6 and $Li_7P_3S_{11}$ have much higher predicted $\beta_{PBE,optB88}$ of 5.28×10^{-5} K^{-1} and 4.07×10^{-5} K^{-1}, respectively. A slightly higher volume expansion is predicted for Li_3YCl_6 by optB88 compared to PBE.

3.4. Ionic conductivity

Fig. 5 shows the Arrhenius plots for the three LSCs from MD simulations performed using the MTPs and a summary of the derived activation energies (E_a) and conductivities at room temperature (σ_{300K}) in comparison with experiments and previous AIMD simulations. From the MTP$_{PBE, optB88}$ Arrhenius plots (filled markers and solid lines), it is immediately apparent that all three LSCs do not exhibit a single linear Arrhenius regime, which is the common assumption made when extrapolating high-temperature (HT) AIMD simulations to room temperature. Transitions between a HT quasi-linear regime with lower E_a and a low-temperature (LT) quasi-linear regime with higher E_a occur at ~ 450 K, 425 K and 400 K for LLTO, Li_3YCl_6 and $Li_7P_3S_{11}$, respectively. In all cases, the MTP$_{PBE, optB88}$ predicted σ_{300K} and E_a are in remarkably good agreement with previously reported experimental values for all three LSCs. In particular, while previous HT AIMD simulations predicted an extraordinarily high σ^*_{300K} of 57 mS cm^{-1} for $Li_7P_3S_{11}$, the MTP$_{PBE, optB88}$ predicted σ^*_{300K} and σ_{300K} are only 6.50 and 7.51 mS cm^{-1}, much closer to the 4−17 mS cm^{-1} that have been reported experimentally thus far [10−13]. We further note that the MTP$_{PBE, optB88}$ HT E_a are also consistent with those obtained from previous HT AIMD simulations for Li_3YCl_6 [29] and $Li_7P_3S_{11}$ [13]. The Li_3YCl_6 LSC has only been experimentally studied at 230−360 K. Our MTP$_{PBE, optB88}$ MD simulations predict that Li_3YCl_6 would undergo a transition to a lower E_a regime at around 425 K; a prediction that would need to be verified by further experiments from the community.

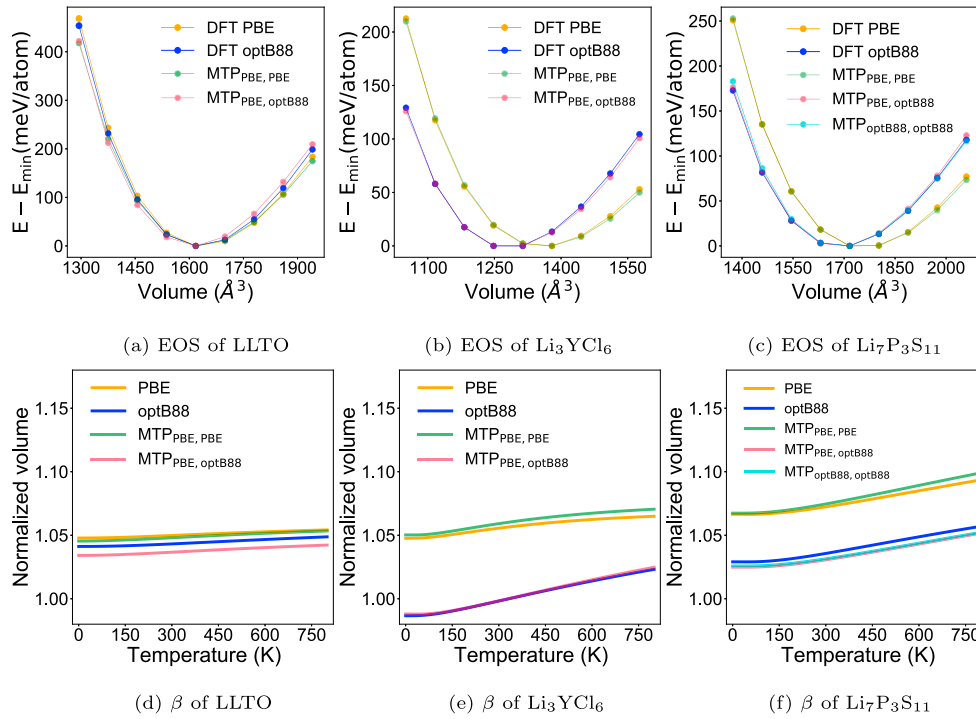The Haven ratios (H_R) at 300 K are 0.68, 0.34 and 0.87 for LLTO,

(a) EOS of LLTO   (b) EOS of Li$_3$YCl$_6$ (c) EOS of Li$_7$P$_3$S$_{11}$

(d) β of LLTO   (e) β of Li$_3$YCl$_6$ (f) β of Li$_7$P$_3$S$_{11}$

Fig. 4. Equations of state at 0 K (a, b, c) and QHA thermal volume expansion β (d, e, f) of LLTO, Li$_3$YCl$_6$ and Li$_7$P$_3$S$_{11}$ calculated from DFT and MTPs. The volumes in the β plots (d, e, f) are normalized with respect to the experimentally measured volumes at room temperatures [9,21,53].

Li$_3$YCl$_6$ and Li$_7$P$_3$S$_{11}$, respectively. There are no existing reports of the Haven ratios for these LSCs to the authors' knowledge. However, LLTO has been experimentally reported to possess highly correlated motions at room temperature [75], consistent with the computed H_R of 0.68. Further, our calculated H_R for Li$_7$P$_3$S$_{11}$ also lies in between the AIMD simulated H_R (0.42, 0.53) [76] and NMR measured H_R (in the order of 1) [77] of Li$_{10}$GeP$_2$S$_{12}$, another sulfide LSC.

We also note that the MTP$_{PBE, optB88}$ and MTP$_{PBE, PBE}$ yield fundamentally different results for Li$_3$YCl$_6$ and Li$_7$P$_3$S$_{11}$. In both cases, the MTP$_{PBE, PBE}$ simulations do not predict any transitions between quasi-linear Arrhenius regimes in the simulation temperature range of 300−600 K. The activation energies E_a and room temperature ionic conductivities σ_{300K} are also severely underestimated and overestimated, respectively, compared to experiments, similar to prior AIMD simulations using the PBE functional. The poor performance of the PBE-based MTP and AIMD simulations can be traced to the substantial overestimation of the lattice parameters by the PBE functional, which can lead to lower activation barriers and higher ionic conductivities [23,78]. It should be noted that we cannot rule out the possibility that the observed transitions between quasi-Arrhenius regimes are an artifact of the DFT functional used in generating the training data, i.e., optB88, but the generally improved agreement between the predicted room-temperature ionic conductivities and experimental values suggest that the transitions are a real phenomenon. It is our hope that future detailed experiments may shed further light on these predictions.

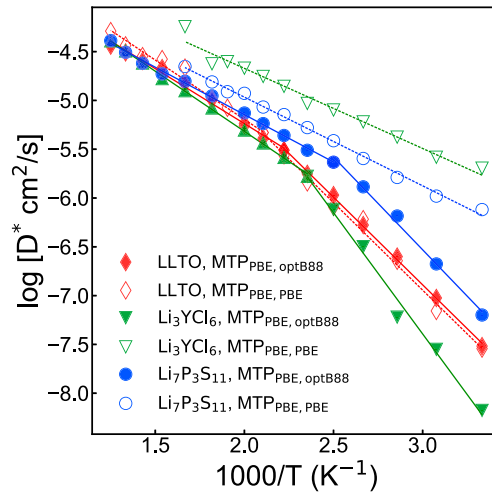### 3.5. Transitions in diffusion mechanisms

To understand the reason behind observed transitions between quasi-linear Arrhenius regimes, we have extracted the trajectories from the MTP$_{PBE, optB88}$ MD simulations of the three LSCs at room temperature and above the transition temperature and plotted them in Fig. 6 and Figure S10-S12. In all three LSCs, a substantial change in the number and variety of diffusion pathways is observed. For LLTO, Li diffusion at 300 K occurs primarily along b and c directions inside the La-poor layer, which agrees well with experimental observations at room temperature [79], but additional diffusion pathways between planes are activated above the transition temperature of 450 K (Fig. 6a). Similarly, Li$_3$YCl$_6$ exhibits quasi-1D diffusion at 300 K and 3D diffusion above the transition temperature of 425 K. For Li$_7$P$_3$S$_{11}$, Li diffusion is already 3D at 300 K but occurs along well-defined pathways. Above the transition temperature of 400 K, additional pathways are activated. The decrease in activation energies E_a can be directly traced to the increase in the variety and dimensionality of diffusion in the three LSCs. The most significant reduction in E_a (~ 0.25 eV) is observed for Li$_3$YCl$_6$, which transitions from a quasi-1D to 3D conductor at around 425 K.

4. Discussion

Briefly, the above results have shown that the discrepancy between computed and experimentally measured ionic conductivities in the literature can be traced to two effects. First, the choice of the DFT functional can lead to substantial errors in the lattice parameters, which can have a large effect on the predicted activation barriers and ionic conductivities. Second, most AIMD simulations of LSCs in the literature were performed at high temperatures in the NVT ensemble to obtain sufficient hop statistics. Not only does this lead to further errors in the lattice parameters, there is also a strong likelihood that these simulations do not capture transitions in quasi-linear Arrhenius regimes occurring at lower temperatures.

These issues can be addressed through carefully-trained ML-IAPs. With a generalizable stepwise workflow for the construction of MTPs for LSCs (see Fig. 2), we have consistently generated training structures sampling a range of local environments (see Figure S8) and fitted MTPs to study LLTO, Li$_3$YCl$_6$ and Li$_7$P$_3$S$_{11}$ LSCs.

	AIMD	MTP$_{PBE,PBE}$	MTP$_{PBE,optB88}$	Experiment
LLTO				
$E_a(eV)$	0.26	0.36 (300-475K)	0.36 (300-450K)	0.40 (300K) [31]
	(900-1800K) [26]	0.24 (475-800K)	0.22 (450-800K)	0.22 (600K) [32]
σ_{300K} (mS cm^{-1})	-	0.97 (σ^*)	1.04 (σ^*), 1.53 (σ)	1-1.3 [31, 53]
Li$_3$YCl$_6$				
$E_a(eV)$	0.19	0.16 (300-600K)	0.49 (300-425K)	0.40 (230-360K) [21]
	(500-900K) [29]		0.24 (425-800K)	
σ_{300K} (mS cm^{-1})	14 [29]	152.66 (σ^*)	0.56 (σ^*), 1.64 (σ)	0.51 [21]
Li$_7$P$_3$S$_{11}$				
$E_a(eV)$	0.19	0.18 (300-600K)	0.38 (300-400K)	0.29 (298-373K) [12]
	(400-1200K) [13]		0.19 (400-800K)	0.18 (300-600K) [13]
σ_{300K} (mS cm^{-1})	57 [13]	67.37 (σ^*)	6.50 (σ^*), 7.51 (σ)	4-17 [10–13]

Fig. 5. (Top) Arrhenius plot for LLTO, Li$_3$YCl$_6$ and Li$_7$P$_3$S$_{11}$ from NPT/MD simulations using MTP$_{PBE,\ PBE}$ (open markers) and MTP$_{PBE,\ optB88}$ (solid markers). The diffusivities were obtained by averaging the mean square displacements from five independent MD simulations at each temperature for at least 1 ns. (Bottom) Room temperature ionic conductivities (σ_{300K}) and activation energies (E_a) for LLTO, Li$_3$YCl$_6$ and Li$_7$P$_3$S$_{11}$, obtained from MD simulations using MTP$_{PBE,\ PBE}$ and MTP$_{PBE,\ optB88}$. For MTP$_{PBE,\ optB88}$, transitions between two quasi-linear Arrhenius regimes were observed for all three LSCs and the E_a for each regime are reported separately. Available AIMD derived values as well as experimental references are also listed.

Our results suggest that the choice of DFT functional used in generating the initial and snapshot training structures is relatively unimportant, but the choice of the DFT functional used in the energy and force evaluations to generate the training data is critically important. Here, we show that the use of the optB88 vdW functional for static energy and force calculations and the ns-scale ML-IAP MD at lower temperatures significantly improve the agreement in lattice parameters, activation energies and room-temperature ionic conductivities of the LSCs with experiments.

These results have broad implications for ML-IAP development strategy. The typical approach in the literature thus far has been to use the same DFT functional in both the generation of training structures as well as energy/force evaluations. Decoupling these two choices allow one to use a relatively cheap computational method such as PBE functional or even other empirical potentials, for the most expensive step of generating training structures, while using a more expensive but accurate computational method, e.g., SCAN or HSE, for the static energy and force evaluations. While the generation of the DFT training data dominates the computational effort in developing ML-IAPs, it should be noted that the ML-IAPs themselves are many orders of magnitude computationally less expensive than DFT calculations, and more importantly, scales linearly with respect to the number of atoms (see Table S3). It is this linear scaling property, while retaining close to DFT accuracy in energies and forces, that enables the simulations of large systems at long time scales in this work.

Our results also have significant implications for LSC development. For all three LSCs investigated, a transition between diffusive regimes is observed at relatively low temperatures (400−450 K). In most cases, the activation barriers and ionic conductivities that have been experimentally measured correspond to the low-temperature regime. One potential avenue for further enhancing the ionic conductivities of these and other LSCs is to attempt to stabilize the high-temperature, lower activation energy diffusion regimes at room temperature. This may be achieved by quenching from higher temperatures, compositional modifications (e.g., dopants or substitutions), or mechanical modifications (e.g., introducing strain). By developing ML-IAPs using the approach outlined in this work, MD simulations can provide critical guidance on potential pathways for further LSC optimization.

5. Conclusions

To conclude, we have shown that MTPs trained using optB88 energies and forces can successfully reproduce the experimental lattice parameters, activation energies and room temperature ionic
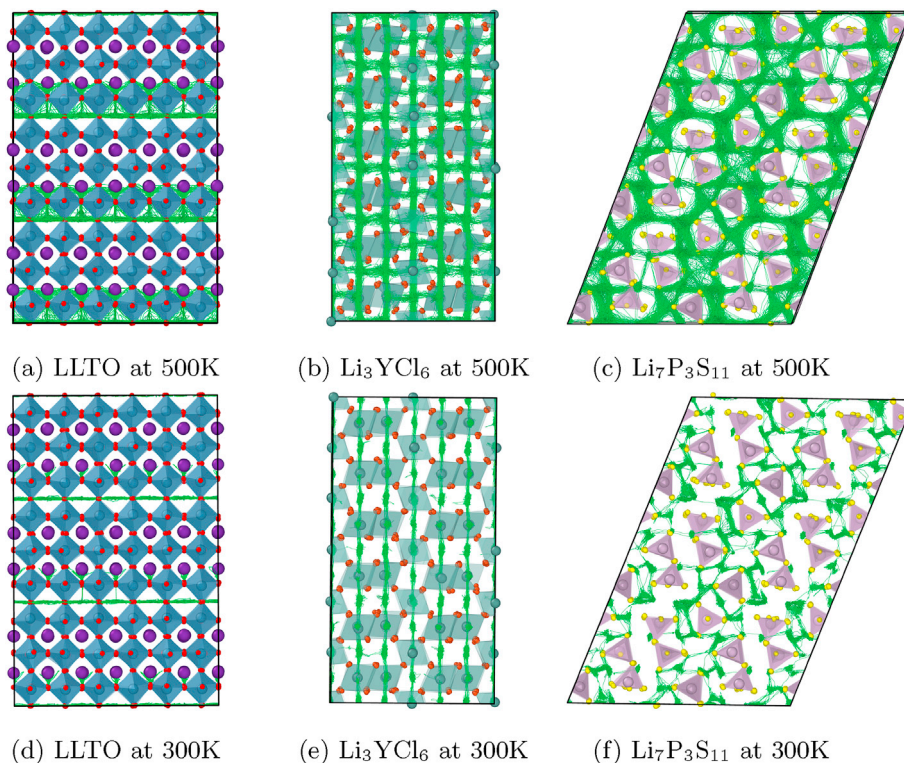
(a) LLTO at 500K   (b) Li_3YCl_6 at 500K   (c) $Li_7P_3S_{11}$ at 500K

(d) LLTO at 300K   (e) Li_3YCl_6 at 300K   (f) $Li_7P_3S_{11}$ at 300K

Fig. 6. Li trajectories (colored as green) from $MTP_{PBE, optB88}$ MD simulations of the LLTO, Li_3YCl_6 and $Li_7P_3S_{11}$ LSCs at room temperature (300 K) and above the transition temperatures. For brevity, only the projection in the crystallographic a-c, b-c and a-c planes are shown for LLTO, Li_3YCl_6 and $Li_7P_3S_{11}$, respectively, at each temperature. The projections in the other crystallographic planes are provided in Figure S10-S12.

conductivities of the LLTO, Li_3YCl_6 and $Li_7P_3S_{11}$ LSCs. In all three LSCs, MD simulations using the trained MTP identify a transition between quasi-linear Arrhenius regimes occurring at relatively low temperatures. These results not only highlight the fundamental limitations in using high-temperature, short time scale AIMD simulations to predict room-temperature properties of materials, but also suggest a potential pathway and strategy to predictive LSC design through the use of machine learning interatomic potentials.

Data availability

The datasets generated and/or analyzed during the current study are available from the corresponding author on reasonable request.

Declaration of competing interest

The authors declare that they have no known competing financial interests or personal relationships that could have appeared to influence the work reported in this paper.

Acknowledgements

Appendix A. Supplementary data

Supplementary data to this article can be found online at https://doi.org/10.1016/j.mtphys.2021.100463.

References

[1] J.-M. Tarascon, M. Armand, Issues and challenges facing rechargeable lithium batteries, Nature 414 (6861) (2001) 359–367, https://doi.org/10.1038/35104644.
[2] M. Armand, J.-M. Tarascon, Building better batteries, Nature 451 (7179) (2008) 652–657, https://doi.org/10.1038/451652a.
[3] K. Xu, Electrolytes and interphases in Li-ion batteries and beyond, Chem. Rev. 114 (23) (2014) 11503–11618, https://doi.org/10.1021/cr500003w.
[4] Y. Wang, W.D. Richards, S.P. Ong, L.J. Miara, J.C. Kim, Y. Mo, G. Ceder, Design principles for solid-state lithium superionic conductors, Nat. Mater. 14 (10) (2015) 1026–1031, https://doi.org/10.1038/nmat4369.
[5] N. Kamaya, K. Homma, Y. Yamakawa, M. Hirayama, R. Kanno, M. Yonemura, T. Kamiyama, Y. Kato, S. Hama, K. Kawamoto, A. Mitsui, A lithium superionic conductor, Nat. Mater. 10 (9) (2011) 682–686, https://doi.org/10.1038/nmat3066.
[6] P. Bron, S. Johansson, K. Zick, J. Schmedt auf der Günne, S. Dehnen, B. Roling, Li$_{10}$ SnP $_2$ S $_{12}$: an affordable lithium superionic conductor, J. Am. Chem. Soc. 135 (42) (2013) 15694–15697, https://doi.org/10.1021/ja407393y.
[7] J.M. Whiteley, J.H. Woo, E. Hu, K.-W. Nam, S.-H. Lee, Empowering the lithium metal battery through a silicon-based superionic conductor, J. Electrochem. Soc. 161 (12) (2014) A1812–A1817, https://doi.org/10.1149/2.0501412jes.
[8] Y. Kato, S. Hori, T. Saito, K. Suzuki, M. Hirayama, A. Mitsui, M. Yonemura, H. Iba, R. Kanno, High-power all-solid-state batteries using sulfide superionic conductors, Nature Energy 1 (4) (2016) 16030, https://doi.org/10.1038/nenergy.2016.30.
[9] H. Yamane, M. Shibata, Y. Shimane, T. Junke, Y. Seino, S. Adams, K. Minami, A. Hayashi, M. Tatsumisago, Crystal structure of a superionic conductor, Li7P3S11, Solid State Ionics 178 (15–18) (2007) 1163–1167, https://doi.org/10.1016/j.ssi.2007.05.020.

[10] Y. Seino, T. Ota, K. Takada, A. Hayashi, M. Tatsumisago, A sulphide lithium super ion conductor is superior to liquid ion conductors for use in recharge-able batteries, Energy Environ. Sci. 7 (2) (2014) 627−631, https://doi.org/10.1039/C3EE41655K.

[11] S. Wenzel, D.A. Weber, T. Leichtweiss, M.R. Busche, J. Sann, J. Janek, Interphase formation and degradation of charge transfer kinetics between a lithium metal anode and highly crystalline Li7P3S11 solid electrolyte, Solid State Ionics 286 (2016) 24−33, https://doi.org/10.1016/j.ssi.2015.11.034.

[12] M.R. Busche, D.A. Weber, Y. Schneider, C. Dietrich, S. Wenzel, T. Leichtweiss, D. Schröder, W. Zhang, H. Weigand, D. Walter, S.J. Sedlmaier, D. Houtarde, L.F. Nazar, J. Janek, *In situ* monitoring of fast Li-ion conductor Li $_7$ P $_3$ S $_{11}$ crystallization inside a hot-press setup, Chem. Mater. 28 (17) (2016) 6152−6165, https://doi.org/10.1021/acs.chemmater.6b02163.

[13] I.-H. Chu, H. Nguyen, S. Hy, Y.-C. Lin, Z. Wang, Z. Xu, Z. Deng, Y.S. Meng, S.P. Ong, Insights into the performance limits of the Li $_7$ P $_3$ S $_{11}$ superionic conductor: a combined first-principles and experimental study, ACS Appl. Mater. Interfaces 8 (12) (2016) 7843−7853, https://doi.org/10.1021/acsami.6b00833.

[14] M. Tachez, J. Maluganı, R. Mercier, G. Robert, Ionic conductivity of and phase transition in lithium thiophosphate Li3PS4, Solid State Ionics 14 (3) (1984) 181−185, https://doi.org/10.1016/0167-2738(84)90097-3.

[15] Z. Liu, W. Fu, E.A. Payzant, X. Yu, Z. Wu, N.J. Dudney, J. Kiggans, K. Hong, A.J. Rondinone, C. Liang, Anomalous high ionic conductivity of nanoporous β-Li $_3$ PS $_4$, J. Am. Chem. Soc. 135 (3) (2013) 975−978, https://doi.org/10.1021/ja3110895.

[16] T. Yamada, S. Ito, R. Omoda, T. Watanabe, Y. Aihara, M. Agostini, U. Ulissi, J. Hassoun, B. Scrosati, All solid-state lithium−sulfur battery using a glass-type P $_2$ S $_5$ −Li $_2$ S electrolyte: benefits on anode kinetics, J. Electrochem. Soc. 162 (4) (2015) A646−A651, https://doi.org/10.1149/2.0441504jes.

[17] R. Murugan, V. Thangadurai, W. Weppner, Fast lithium ion conduction in garnet-type Li7La3Zr2O12, Angew. Chem. Int. Ed. 46 (41) (2007) 7778−7781, https://doi.org/10.1002/anie.200701144.

[18] Y.W. Hu, I.D. Raistrick, R.A. Huggins, Ionic conductivity of lithium orthosili-cate—lithium phosphate solid solutions, J. Electrochem. Soc. 124 (8) (1977) 1240−1242, https://doi.org/10.1149/1.2133537.

[19] J. Kuwano, A. West, New Li+ ion conductors in the system, Li4GeO4-Li3VO4, Mater. Res. Bull. 15 (11) (1980) 1661−1667, https://doi.org/10.1016/0025-5408(80)90249-4.

[20] P. Bruce, A. West, Ionic conductivity of LISICON solid solutions, Li2+2xZn1-xGeO4, J. Solid State Chem. 44 (3) (1982) 354−365, https://doi.org/10.1016/0022-4596(82)90383-8.

[21] T. Asano, A. Sakai, S. Ouchi, M. Sakaida, A. Miyazaki, S. Hasegawa, Solid halide electrolytes with high lithium-ion conductivity for application in 4 V class bulk-type All-solid-state batteries, Adv. Mater. 30 (44) (2018) 1803075, https://doi.org/10.1002/adma.201803075.

[22] Y. Mo, S.P. Ong, G. Ceder, First principles study of the Li $_{10}$ GeP $_2$ S $_{12}$ lithium super ionic conductor material, Chem. Mater. 24 (1) (2012) 15−17, https://doi.org/10.1021/cm203303y.

[23] S.P. Ong, Y. Mo, W.D. Richards, L. Miara, H.S. Lee, G. Ceder, Phase stability, electrochemical stability and ionic conductivity of the Li $_{10±1}$ MP $_2$ X $_{12}$ (M = Ge, Si, Sn, Al or P, and X = O, S or Se) family of superionic conductors, Energy Environ. Sci. 6 (1) (2013) 148−156, https://doi.org/10.1039/C2EE23355J.

[24] L.J. Miara, S.P. Ong, Y. Mo, W.D. Richards, Y. Park, J.-M. Lee, H.S. Lee, G. Ceder, Effect of Rb and Ta doping on the ionic conductivity and stability of the garnet Li $_{7+2 x − y}$ (La $_{3− x}$ Rb $_x$)(Zr $_{2− y}$ Ta $_y$)O $_{12}$ (0 ≤ x ≤ 0.375, 0 ≤ y ≤ 1) superionic conductor: a first principles investigation, Chem. Mater. 25 (15) (2013) 3048−3055, https://doi.org/10.1021/cm401232r.

[25] Z. Deng, B. Radhakrishnan, S.P. Ong, Rational composition optimization of the lithium-rich Li $_3$ OCl $_{1−x}$ Br $_x$ anti-perovskite superionic conductors, Chem. Mater. 27 (10) (2015) 3749−3755, https://doi.org/10.1021/acs.chemmater.5b00988.

[26] X. He, Y. Zhu, Y. Mo, Origin of fast ion diffusion in super-ionic conductors, Nat. Commun. 8 (1) (2017) 15893, https://doi.org/10.1038/ncomms15893.

[27] Z. Zhu, I.-H. Chu, S.P. Ong, Li $_3$ Y(PS $_4$) $_2$ and Li $_5$ PS $_4$ Cl $_2$: new lithium superionic conductors predicted from silver thiophosphates using efficiently tiered ab initio molecular dynamics simulations, Chem. Mater. 29 (6) (2017) 2474−2484, https://doi.org/10.1021/acs.chemmater.6b04049.

[28] Z. Deng, Z. Zhu, I.-H. Chu, S.P. Ong, Data-driven first-principles methods for the study and design of alkali superionic conductors, Chem. Mater. 29 (1) (2017) 281−288, https://doi.org/10.1021/acs.chemmater.6b02648.

[29] S. Wang, Q. Bai, A.M. Nolan, Y. Liu, S. Gong, Q. Sun, Y. Mo, Lithium chlorides and bromides as promising solid-state chemistries for fast ion conductors with good electrochemical stability, Angew. Chem. Int. Ed. 58 (24) (2019) 8039−8043, https://doi.org/10.1002/anie.201901938.

[30] X. He, Y. Zhu, A. Epstein, Y. Mo, Statistical variances of diffusional properties from ab initio molecular dynamics simulations, npj Computational Materials 4 (1) (2018) 18, https://doi.org/10.1038/s41524-018-0074-y.

[31] Y. Inaguma, C. Liquan, M. Itoh, T. Nakamura, T. Uchida, H. Ikuta, M. Wakihara, High ionic conductivity in lithium lanthanum titanate, Solid State Commun. 86 (10) (1993) 689−693, https://doi.org/10.1016/0038-1098(93)90841-A.

[32] T. Šalkus, E. Kazakevičius, A. Kežionis, A. Orliukas, J. Badot, O. Bohnke, Determination of the non-Arrhenius behaviour of the bulk conductivity of fast ionic conductors LLTO at high temperature, Solid State Ionics 188 (1) (2011) 69−72, https://doi.org/10.1016/j.ssi.2010.09.005.

[33] O. Kwon, M. Hirayama, K. Suzuki, Y. Kato, T. Saito, M. Yonemura, T. Kamiyama, R. Kanno, Synthesis, structure, and conduction mechanism of the lithium superionic conductor Li $_{10+\delta}$ Ge $_{1+\delta}$ P $_{2-\delta}$ S $_{12}$, J. Mater. Chem. 3 (1) (2015) 438−446, https://doi.org/10.1039/C4TA05231E.

[34] J.P. Perdew, K. Burke, M. Ernzerhof, Generalized gradient approximation made simple, Phys. Rev. Lett. 77 (18) (1996) 3865−3868, https://doi.org/10.1103/PhysRevLett.77.3865.

[35] J. Heyd, J.E. Peralta, G.E. Scuseria, R.L. Martin, Energy band gaps and lattice parameters evaluated with the Heyd-Scuseria-Ernzerhof screened hybrid functional, J. Chem. Phys. 123 (17) (2005) 174101, https://doi.org/10.1063/1.2085170.

[36] J. Klimeš, D.R. Bowler, A. Michaelides, Van der Waals density functionals applied to solids, Phys. Rev. B 83 (19) (2011) 195131, https://doi.org/10.1103/PhysRevB.83.195131.

[37] A. Moradabadi, P. Kaghazchi, Effect of lattice and dopant−induced strain on the conductivity of solid electrolytes: application of the elastic dipole method, Materialia 9 (2020) 100607, https://doi.org/10.1016/j.mtla.2020.100607.

[38] J. Behler, M. Parrinello, Generalized neural-network representation of high-dimensional potential-energy surfaces, Phys. Rev. Lett. 98 (14) (2007) 146401, https://doi.org/10.1103/PhysRevLett.98.146401.

[39] A.P. Bartók, M.C. Payne, R. Kondor, G. Csányi, Gaussian approximation po-tentials: the accuracy of quantum mechanics, without the electrons, Phys. Rev. Lett. 104 (13) (2010) 136403, https://doi.org/10.1103/PhysRevLett.104.136403.

[40] A. Thompson, L. Swiler, C. Trott, S. Foiles, G. Tucker, Spectral neighbor analysis method for automated generation of quantum-accurate interatomic poten-tials, J. Comput. Phys. 285 (2015) 316−330, https://doi.org/10.1016/j.jcp.2014.12.018.

[41] A.V. Shapeev, Moment tensor potentials: a class of systematically improvable interatomic potentials, Multiscale Model. Simul. 14 (3) (2016) 1153−1173, https://doi.org/10.1137/15M1054183.

[42] H. Wang, L. Zhang, J. Han, W. E, DeePMD-kit: a deep learning package for many-body potential energy representation and molecular dynamics, Com-put. Phys. Commun. 228 (2018) 178−184, https://doi.org/10.1016/j.cpc.2018.03.016.

[43] C. Chen, Z. Deng, R. Tran, H. Tang, I.-H. Chu, S.P. Ong, Accurate force field for molybdenum by machine learning large materials data, Physical Review Materials 1 (4) (2017): 043603, https://doi.org/10.1103/PhysRevMaterials.1.043603.

[44] W. Li, Y. Ando, E. Minamitani, S. Watanabe, Study of Li atom diffusion in amorphous Li3PO4 with neural network potential, J. Chem. Phys. 147 (21) (2017) 214106, https://doi.org/10.1063/1.4997242.

[45] X.-G. Li, C. Hu, C. Chen, Z. Deng, J. Luo, S.P. Ong, Quantum-accurate spectral neighbor analysis potential models for Ni-Mo binary alloys and fcc metals, Phys. Rev. B 98 (9) (2018): 094104, https://doi.org/10.1103/PhysRevB.98.094104.

[46] Z. Deng, C. Chen, X.-G. Li, S.P. Ong, An electrostatic spectral neighbor analysis potential for lithium nitride, npj Computational Materials 5 (1) (2019) 75, https://doi.org/10.1038/s41524-019-0212-1.

[47] X.-G. Li, C. Chen, H. Zheng, Y. Zuo, S.P. Ong, Complex strengthening mecha-nisms in the NbMoTaW multi-principal element alloy, npj Computational Materials 6 (1) (2020) 70, https://doi.org/10.1038/s41524-020-0339-0.

[48] Y. Zuo, C. Chen, X. Li, Z. Deng, Y. Chen, J. Behler, G. Csányi, A.V. Shapeev, A.P. Thompson, M.A. Wood, S.P. Ong, Performance and cost assessment of machine learning interatomic potentials, J. Phys. Chem. 124 (4) (2020) 731−745, https://doi.org/10.1021/acs.jpca.9b08723.

[49] C. Wang, K. Aoyagi, P. Wisesa, T. Mueller, Lithium ion conduction in cathode coating materials from on-the-fly machine learning, Chem. Mater. 32 (9) (2020) 3741−3752, https://doi.org/10.1021/acs.chemmater.9b04663.

[50] J. Huang, L. Zhang, H. Wang, J. Zhao, J. Cheng, W. E, Deep Potential Generation Scheme and Simulation Protocol for the Li10GeP2S12-type Superionic Con-ductors, arXiv:2006.03320 [cond-mat, physics:physics]arXiv, 2006, 03320.

[51] K. Gubaev, E.V. Podryabinkin, G.L. Hart, A.V. Shapeev, Accelerating high-throughput searches for new alloys with active learning of interatomic po-tentials, Comput. Mater. Sci. 156 (2019) 148−156, https://doi.org/10.1016/j.commatsci.2018.09.031.

[52] J. Klimeš, D.R. Bowler, A. Michaelides, Chemical accuracy for the van der Waals density functional, J. Phys. Condens. Matter 22 (2) (2010): 022201, https://doi.org/10.1088/0953-8984/22/2/022201.

[53] Y. Harada, Lithium ion conductivity of polycrystalline perovskite La0.67-xLi3xTiO3 with ordered and disordered arrangements of the A-site ions, Solid State Ionics 108 (1−4) (1998) 407−413, https://doi.org/10.1016/S0167-2738(98)00070-8.

[54] Y. Harada, Order−disorder of the A-site ions and lithium ion conductivity in the perovskite solid solution La0.67-xLi3xTiO3 (x=0.11), Solid State Ionics 121 (1−4) (1999) 245−251, https://doi.org/10.1016/S0167-2738(99)00043-0.

[55] D. Qian, B. Xu, H.-M. Cho, T. Hatsukade, K.J. Carroll, Y.S. Meng, Lithium lanthanum titanium oxides: a fast ionic conductive coating for lithium-ion battery cathodes, Chem. Mater. 24 (14) (2012) 2744−2751, https://doi.org/10.1021/cm300929r.

[56] Y.Q. Cheng, Z.H. Bi, A. Huq, M. Feygenson, C.A. Bridges, M.P. Paranthaman, B.G. Sumpter, An integrated approach for structural characterization of complex solid state electrolytes: the case of lithium lanthanum titanate, J. Mater. Chem. 2 (7) (2014) 2418, https://doi.org/10.1039/c3ta14433j.

[57] M. Romero, R. Faccio, S. Vázquez, S. Davyt, Á.W. Mombrú, Experimental and theoretical Raman study on the structure and microstructure of

Li0.30La0.57TiO3 electrolyte prepared by the sol-gel method in acetic medium, Ceram. Int. 42 (14) (2016) 15414–15422, https://doi.org/10.1016/j.ceramint.2016.06.192.

[58] P.E. Blöchl, Projector augmented-wave method, Phys. Rev. B 50 (24) (1994) 17953–17979, https://doi.org/10.1103/PhysRevB.50.17953.

[59] G. Kresse, J. Furthmüller, Efficient iterative schemes for *ab initio* total-energy calculations using a plane-wave basis set, Phys. Rev. B 54 (16) (1996) 11169–11186, https://doi.org/10.1103/PhysRevB.54.11169.

[60] A. Jain, S.P. Ong, G. Hautier, W. Chen, W.D. Richards, S. Dacek, S. Cholia, D. Gunter, D. Skinner, G. Ceder, K.A. Persson, Commentary: the Materials Project: a materials genome approach to accelerating materials innovation, Apl. Mater. 1 (1) (2013): 011002, https://doi.org/10.1063/1.4812323.

[61] S. Nosé, A unified formulation of the constant temperature molecular dynamics methods, J. Chem. Phys. 81 (1) (1984) 511–519, https://doi.org/10.1063/1.447334.

[62] W.G. Hoover, Canonical dynamics: equilibrium phase-space distributions, Phys. Rev. 31 (3) (1985) 1695–1697, https://doi.org/10.1103/PhysRevA.31.1695.

[63] S.P. Ong, W.D. Richards, A. Jain, G. Hautier, M. Kocher, S. Cholia, D. Gunter, V.L. Chevrier, K.A. Persson, G. Ceder, Python Materials Genomics (pymatgen): a robust, open-source python library for materials analysis, Comput. Mater. Sci. 68 (2013) 314–319, https://doi.org/10.1016/j.commatsci.2012.10.028.

[64] A. Jain, S.P. Ong, W. Chen, B. Medasani, X. Qu, M. Kocher, M. Brafman, G. Petretto, G.-M. Rignanese, G. Hautier, D. Gunter, K.A. Persson, FireWorks: a dynamic workflow system designed for high-throughput applications: FireWorks: a dynamic workflow system designed for high-throughput applications, Concurrency Comput. Pract. Ex. 27 (17) (2015) 5037–5059, https://doi.org/10.1002/cpe.3505.

[65] I. Novoselov, A. Yanilkin, A. Shapeev, E. Podryabinkin, Moment tensor potentials as a promising tool to study diffusion processes, Comput. Mater. Sci. 164 (2019) 46–56, https://doi.org/10.1016/j.commatsci.2019.03.049.

[66] E.V. Podryabinkin, E.V. Tikhonov, A.V. Shapeev, A.R. Oganov, Accelerating crystal structure prediction by machine-learning interatomic potentials with active learning, Phys. Rev. B 99 (6) (2019): 064114, https://doi.org/10.1103/PhysRevB.99.064114.

[67] I.S. Novikov, Y.V. Suleimanov, A.V. Shapeev, Automated calculation of thermal rate coefficients using ring polymer molecular dynamics and machine-learning interatomic potentials with active learning, Phys. Chem. Chem. Phys. 20 (46) (2018) 29503–29512, https://doi.org/10.1039/C8CP06037A.

[68] E.V. Podryabinkin, A.V. Shapeev, Active learning of linearly parametrized interatomic potentials, Comput. Mater. Sci. 140 (2017) 171–180, https://doi.org/10.1016/j.commatsci.2017.08.031.

[69] S. Plimpton, Fast parallel algorithms for short-range molecular dynamics, J. Comput. Phys. 117 (1) (1995) 1–19, https://doi.org/10.1006/jcph.1995.1039.

[70] C. Chen, Y. Zuo, W. Ye, S.P. Ong, Maml - Materials Machine Learning Package, 2020. https://github.com/materialsvirtuallab/maml.

[71] X. Gonze, C. Lee, Dynamical matrices, Born effective charges, dielectric permittivity tensors, and interatomic force constants from density-functional perturbation theory, Phys. Rev. B 55 (16) (1997) 10355–10368, https://doi.org/10.1103/PhysRevB.55.10355.

[72] A. Togo, I. Tanaka, First principles phonon calculations in materials science, Scripta Mater. 108 (2015) 1–5, https://doi.org/10.1016/j.scriptamat.2015.07.021.

[73] A. Van der Ven, Z. Deng, S. Banerjee, S.P. Ong, Rechargeable alkali-ion battery materials: theory and computation, Chem. Rev. 120 (14) (2020) 6977–7019, https://doi.org/10.1021/acs.chemrev.9b00601.

[74] T. Okumura, A. Dodomi, M. Saito, J. Kuwano, Computational simulations of Li ion conduction in (Li,La)TiO$_3$, Key Eng. Mater. 320 (2006) 275–278, https://doi.org/10.4028/www.scientific.net/KEM.320.275.

[75] O. Bohnke, The fast lithium-ion conducting oxides Li3xLa2/3-xTiO3 from fundamentals to application, Solid State Ionics 179 (1–6) (2008) 9–15, https://doi.org/10.1016/j.ssi.2007.12.022.

[76] A. Marcolongo, N. Marzari, Ionic correlations and failure of Nernst-Einstein relation in solid-state electrolytes, Physical Review Materials 1 (2) (2017): 025402, https://doi.org/10.1103/PhysRevMaterials.1.025402.

[77] A. Kuhn, V. Duppel, B.V. Lotsch, Tetragonal Li10GeP2S12 and Li7GePS8 — exploring the Li ion dynamics in LGPS Li electrolytes, Energy Environ. Sci. 6 (12) (2013) 3548, https://doi.org/10.1039/c3ee41728j.

[78] A. Kuhn, O. Gerbig, C. Zhu, F. Falkenberg, J. Maier, B.V. Lotsch, A new ultrafast superionic Li-conductor: ion dynamics in Li$_{11}$Si$_2$PS$_{12}$ and comparison with other tetragonal LGPS-type electrolytes, Phys. Chem. Chem. Phys. 16 (28) (2014) 14669–14674, https://doi.org/10.1039/C4CP02046D.

[79] C. Ma, Y. Cheng, K. Chen, J. Li, B.G. Sumpter, C.-W. Nan, K.L. More, N.J. Dudney, M. Chi, Mesoscopic framework enables facile ionic transport in solid electrolytes for Li batteries, Advanced Energy Materials 6 (11) (2016) 1600053, https://doi.org/10.1002/aenm.201600053.